ANIMAL LOCOMOTION

Tunable stiffness enables fast and efficient swimming in fish-like robots

Q. Zhong[1]*, J. Zhu[1], F. E. Fish[2], S. J. Kerr[2], A. M. Downs[2], H. Bart-Smith[1], D. B. Quinn[1,3]*

Fish maintain high swimming efficiencies over a wide range of speeds. A key to this achievement is their flexibility, yet even flexible robotic fish trail real fish in terms of performance. Here, we explore how fish leverage tunable flexibility by using their muscles to modulate the stiffness of their tails to achieve efficient swimming. We derived a model that explains how and why tuning stiffness affects performance. We show that to maximize efficiency, muscle tension should scale with swimming speed squared, offering a simple tuning strategy for fish-like robots. Tuning stiffness can double swimming efficiency at tuna-like frequencies and speeds (0 to 6 hertz; 0 to 2 body lengths per second). Energy savings increase with frequency, suggesting that high-frequency fish-like robots have the most to gain from tuning stiffness.

INTRODUCTION

For decades, scientists and engineers have tried to understand how fish maintain such high swimming efficiencies over such a wide range of speeds. One of the "overarching" (*1*) themes in this quest has been flexibility. Fish are highly flexible: When limp, their bodies can be as pliable as loose-leaf paper [e.g., flexural rigidity $EI \approx 1$ to 2 N mm^2 (*2*)]. Theories, simulations, and experiments all show that flexibility can improve performance (*3*–*7*), yet fish-inspired robots—even those that are flexible—trail real fish in terms of speed and efficiency (*8*–*11*). Here, we explore a missing feature that perpetuates this performance gap: tunable stiffness.

It has been hypothesized that no one stiffness optimizes a fish's performance, so fish tune their stiffness as they swim using active muscle tensioning (*12*). Muscle activity in sunfish (*Lepomis macrochirus*) (*13*), for example, suggests speed-dependent tail stiffening. Electrical stimulations of deceased bass (*Micropterus salmoides*) (*14*) and eels (*Anguilla rostra*) (*2*) suggest that muscle tensioning could triple a fish's effective stiffness. How muscles actively modulate stiffness is not well understood (*1*), but proposed mechanisms approximating muscle behavior include bilateral tendon tensioning (*14*, *15*) and curvature control (*16*). Because it is nearly impossible to measure the stiffness of live fishes as they swim, two key questions remain unanswered: What are the energetic advantages of tuning stiffness, and how should stiffness be tuned to maximize efficiency during free swimming?

These questions apply equally to robotic fish, where stiffness-tuning mechanisms already exist. Robots can tune stiffness offline by swapping in/out passive stiffness elements (*17*, *18*) or online by using adjustable linear/leaf springs (*19*, *20*), bilateral soft actuators (*21*), artificial tendons (*22*), electrorheological modulation (*23*), or cyber-physical motor braking (*24*). These studies showed how stiffness-tuning mechanisms have pros and cons involving degrees of freedom, compactness, simplicity, and modularity. They also demonstrated how tuning stiffness can increase thrust production. It is still unclear, however, what stiffness-tuning strategies are best and how they relate to swimming efficiency.

Using a combination of modeling and experiments, we quantified the energetic benefits of tuning stiffness over a range of swimming speeds. In particular, we found that tuna-like robots should tension their tail joint with a force proportional to their speed squared. The mechanism is analogous to a continuously variable transmission, where a car improves its efficiency by tuning gear ratio with driving speed. Our model explains how fish-like robots could emulate fish, who use the same gait over a wide range of speeds (*25*), and why robots with a fixed amount of flexibility may never surpass fish in terms of performance.

RESULTS

Tuna tails inspire theory and experiments with tunable stiffness

We chose tuna (family Scombridae) for our model organism, because they are high-speed, high-efficiency apex predators (*26*, *27*). Tuna have paired lateral tendons that pass from anterior muscles through the tail joint (peduncle) and onto tail/caudal fin rays (Fig. 1A) (*28*). As the sum force on these tendons increases, so too does the effective stiffness of the tail (Fig. 1B). Muscles and tendons often exhibit strut- or spring-like behaviors (*29*, *30*), and we speculated that a simple mechanical model could explain stiffness tuning in a tuna-like robot as it pertains to performance.

Our biomechanical model recreates the basic stiffening response of real tensioned tuna tails. The model treats the tuna as two parts: a "head" that generates drag and a "tail" that generates thrust (Fig. 1C). The front of the tail pitches back and forth and drives the lateral heaving motions of the tail joint, and the tail joint supports a passive fin that is tensioned by a muscle-inspired spring. In our model, increasing the force on the spring (T_M) increases the effective torsional spring coefficient of the tail joint (Fig. 1D).

To test our theoretical model, we built a tuna-like platform that tunes its own tail stiffness using a motor-driven "muscle" (spring) (Fig. 1E). As with the biological and theoretical tail joint, pulling harder on the spring increases the torsional stiffness of the tail (Fig. 1F). To test the platform over the wide range of kinematics seen in real tuna, we built a custom actuator that pitches our robotic tail at high frequencies (up to 6 Hz) while also tuning amplitude (0° to 35°) and

[1]Department of Mechanical and Aerospace Engineering, University of Virginia, 122 Engineer's Way, Charlottesville, VA 22903, USA. [2]Department of Biology, West Chester University, 730 S High St., West Chester, PA 19383, USA. [3]Department of Electrical and Computer Engineering, University of Virginia, 122 Engineer's Way, Charlottesville, VA 22903, USA.
*Corresponding author. Email: qz4te@virginia.edu (Q.Z.); danquinn@virginia.edu (D.B.Q.)

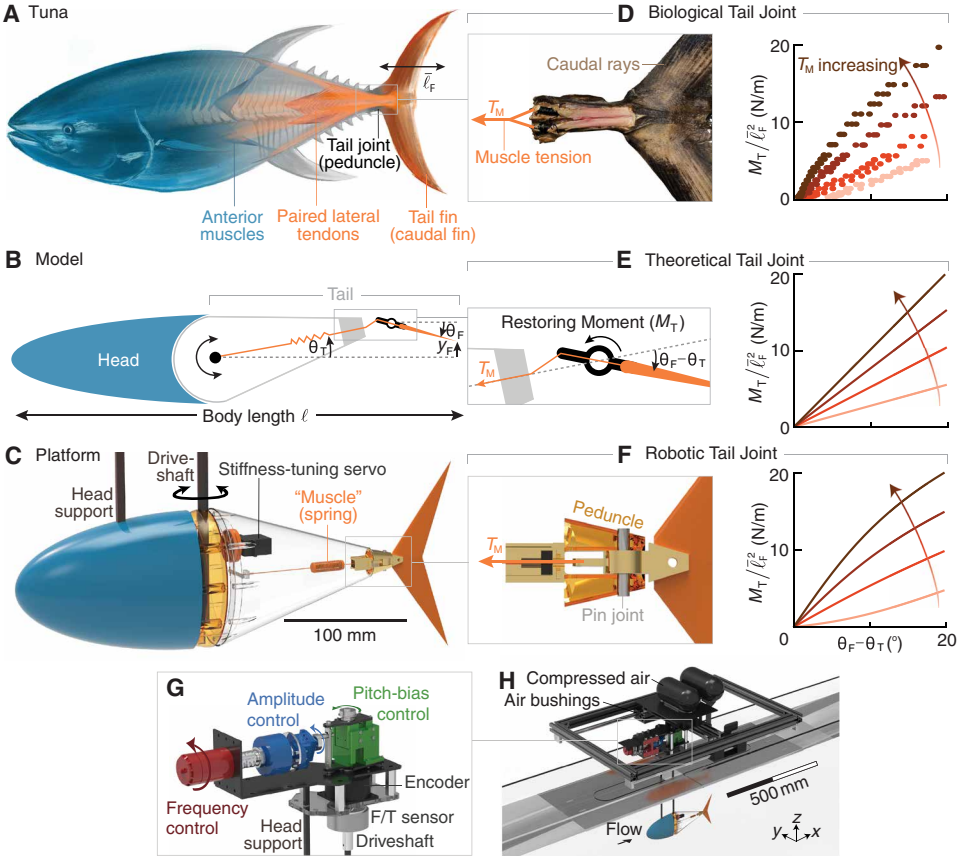

Fig. 1. A tail with tunable stiffness was modeled after tuna. (**A**) In tuna tails, paired lateral tendons connect anterior body muscles to rays of the caudal fin. (**B**) Simplified model: The tail is pitched back and forth at an angle θ_T, and the tail fin responds passively. (**C**) In our platform, a servo tightened a spring to adjust tail stiffness. The robot's head was fixed, whereas its tail was pitched by a driveshaft. (**D**) A dissected tuna tail exhibited behaviors of a tuned torsional spring (see fig. S1 for other tails, $N = 6$). When a force (T_M) was applied to the lateral tendons, the restoring moment of the peduncle rose faster with fin pitch angle (θ_F). (**E** and **F**) The model and robotic tail also behave like tuned springs (one-parameter fit to match tuna tail; eqs. S1.1 and S1.2). (**G**) A Scotch-yoke mechanism adjusted the frequency, amplitude, and pitch bias of the driveshaft. An absolute encoder and a torque sensor recorded mechanical power input. (**H**) The platform was suspended in a recirculating water channel (*W*: 380 mm × *H*: 450 mm × *L*: 1520 mm) and could float in a horizontal plane because of a two-axis air bushing system. See Materials and Methods, movie S1, sections S1.1 to S1.4, and figs. S1 to S6 for details.

pitch bias (0° to 20°) (Fig. 1G). Whereas real fish muscles both tune stiffness and actuate fins (*2*, *13*), our platform uses two separate systems (Fig. 1, E and G), which allows us to decouple active stiffness control from locomotion.

Maintaining high speed and efficiency requires tunable stiffness

To predict swimming speed and efficiency, we combined our biomechanical model with thin airfoil theory (*31*), which gives the forces and torques on heaving/pitching hydrofoils. We treated the tail fin as a hydrofoil whose heave was prescribed by our actuator and whose pitch angle responded passively on the basis of hydrodynamic forces and the spring tension (T_M). To test the model predictions, we tested our tuna-like platform over a grid of tailbeat frequencies and spring tensions (841 total trials) as it self-propelled (Thrust = Drag) in a water channel (Fig. 1H).

We found that swimming speed and efficiency (speed/input power) are highly dependent on tail stiffness. At low frequencies, swimming speed (u) rises linearly with frequency (f) (Fig. 2A), as it does in real fish (*32*). A linear frequency-speed relation implies a constant "stride length," i.e., body lengths traveled per tailbeat, or $u/(f\ell)$ where ℓ is body length. If stiffness stays constant and frequency rises further, then stride length and efficiency begin to decline (Fig. 2A, right). To maintain high efficiency, stiffness must increase with swimming speed. A robot could keep a look-up table of optimal stiffnesses, but such a black-box strategy would have limited scope. We used our model to seek a more physics-driven strategy—one that could be used to explore biological variation and design new generations of robots.

Muscle/spring tension should scale with swimming speed squared

To understand the patterns in efficiency that we observed (Fig. 2B), we considered what dimensionless ratios appear in our model. The amplitude of the tail fin is known to correlate with thrust (*33*). In our model, the lateral position of the tail fin's trailing/distal edge (y_F) behaves like a damped oscillator driven by the prescribed motions [$\theta_T(t)$]

$$\ddot{y}_F = -\frac{16S^2}{9\pi^3}\left(\frac{\pi C_{def}}{2} + \tau^2\right) y_F - \frac{4S}{3\pi}(1 + C_{def})\dot{y}_F + F(\theta_T(t)) \quad (1)$$

where C_{def} is the Theodorsen wake deficiency function (*34*), F is a complex function of the prescribed motions, S is stride length, and τ is a ratio relating muscle tension and swimming speed [$\tau \equiv \gamma\sqrt{T_M/(\bar{\ell}_F^3 u^2)}$ where γ is a constant and $\bar{\ell}_F$ is the tail fin length; details in section S2.1].

The "scaled muscle tension" τ is related to the Cauchy number, which relates elastic forces to hydrodynamic forces (*35*). The appearance of τ in Eq. 1 highlights its importance in the dynamics of the tail fin. Adjusting τ tunes the damped oscillator by changing the spring-like term (first term on the right-hand side) and therefore the resonant frequency of the system. Fish have previously been modeled as driven oscillators (*30*), but here, we offer a direct link between a controllable stiffness parameter (T_M) and swimming performance (e.g., efficiency).

Our model predicts that stride length (S) is a function of scaled muscle tension (τ) and peaks at an intermediate τ value (Fig. 3A). Free-swimming data from our rig corroborate this prediction: the data cluster around a single $S(\tau)$ curve with a local maximum near $\tau = 2.5$ (Fig. 3A). Under this locally optimal condition, the oscillator

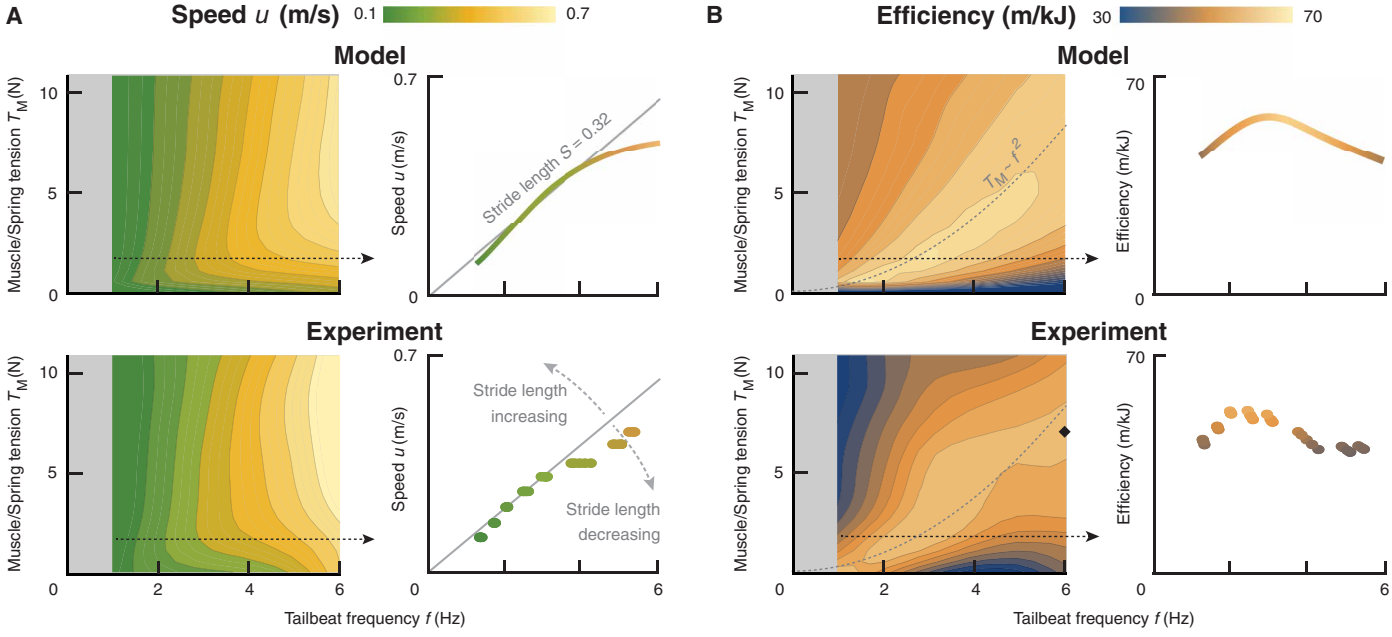

Fig. 2. Swimming speed and efficiency depend on muscle tension and tailbeat frequency. (**A**) Left: Speed is maximized when both frequency and muscle tension are high (contour plot interpolated from 841 points). Right: If muscle tension stays constant (T_M = 1.9 N), then stride length declines at high frequencies. Model is matched to experiment with a one-parameter fit for tail fin thrust coefficient (C_T = 2.4; see section S2.1). (**B**) Left: Efficiency is maximized when muscle tension is tuned for a specific frequency. Ideal tension at F = 6 Hz: 8.7 N (model), 7 ± 0.3 N (experiment, ◆). Right: If muscle tension stays constant, then efficiency peaks at an intermediate frequency.

in Eq. 1 is at resonance (maximal tail amplitude), the stride length and efficiency are maximized, and the tail fin's pitch angle lags its heave by ≈ 90° (Fig. 3B). These results are consistent with previous work: Swimming at resonance maximizes stride length in, for example, robotic lampreys (*36*), and an optimal phase lag of 90° has been observed in hydrofoils with fully prescribed motions (*37*, *38*).

According to our model, an efficient swimmer should tune its stiffness to stay at the τ value yielding the highest stride length. To stay at one value of τ ($\gamma\sqrt{T_M/(\ell_F^3 u^2)}$), the muscle/spring tension must increase with swimming speed squared ($T_M \sim u^2$). Under this condition, stride length is constant, so tension must also increase with frequency squared. This result explains why the ridge of peak efficiencies exists near a curve where $T_M \sim f^2$ (Fig. 2B). In classic elasticity theory, resonant frequencies scale with the square root of stiffness (*39*). In our model, the swimming speed and the resonant frequency are coupled, causing a speed-dependent optimal muscle/spring tension.

Nonlinear wakes induce extra energy costs at high stiffnesses

At high frequencies (f > ≈ 4 Hz), the model begins to overpredict the optimal muscle/spring tension (by 24 ± 5% at 6 Hz; Fig. 2B). To understand why, we used particle image velocimetry (PIV) to map the three-dimensional (3D) flow around our robotic tail (28 stitched layers of cycle-averaged stereo-PIV). On the basis of our efficiency measurements, we considered three cases of scaled muscle tension (τ): one below peak efficiency ("too soft," τ = 1.88), one at peak efficiency ("ideal," τ = 2.68), and one above peak efficiency ("too stiff," τ = 3.96) (Fig. 3A).

As stiffness increases, more vorticity sheds into the wake of the robot's tail fin. As the muscle pulls harder, the maximum angle of attack increases, and the leading edge vortex (LEV) becomes stronger and more detached from the tail fin (Fig. 3C). LEVs are prone to detachment at high angles of attack (*40*), like those present when the tail fin is overstiffened. Attached LEVs can cause transient bursts of thrust (*41*), but detached LEVs can decrease efficiency (*42*, *43*). In the too stiff case, the W-shaped LEV detaches fully and morphs into a ring (Fig. 3C). These wake structures contain lateral kinetic energy that could otherwise have been spent on thrust. Such severe detachment was not present at low frequencies (fig. S9). Despite these wake effects, which slightly shift the optimal muscle/spring tension at high frequencies, the physics-driven tuning strategy ($T_M \sim u^2$) still leads to near-optimal efficiencies (within 5% of the highest efficiency observed at 6 Hz; Fig. 2B).

Real-time stiffness tuning increases swimming efficiency in multispeed missions

To quantify the energetic advantages of stiffness tuning, we tested our platform's ability to carry out multispeed missions. We hung the platform from air bushings so it could move forward and backward (Fig. 1H) and then had it maintain its position against the flow using a proportional-derivative (PD) controller to modulate tailbeat frequency. The flow was ramped up from 0.1 to 0.65 m/s (0.3 to 2 ℓ/s) over 15 min, simulating a 200-m multispeed mission (Fig. 4A). To test the robustness of stiffness tuning, we also added a left-right axis of air bushings so that the platform would recoil laterally (mission 2), programmed the platform to maneuver in a serpentine route (mission 3), and increased its tailbeat amplitude by 33% (mission 4). While swimming, the robotic tail tuned its muscle tension based on what was estimated to optimize efficiency (Fig. 2B). For comparison cases, we fully de-tensioned the spring (T_M effectively zero; "loose"), bolted the tail fin to the tail joint (T_M effectively infinite; "rigid"), and imposed a fixed spring tension chosen for its high efficiency (T_M = 5.5 N; "medium").

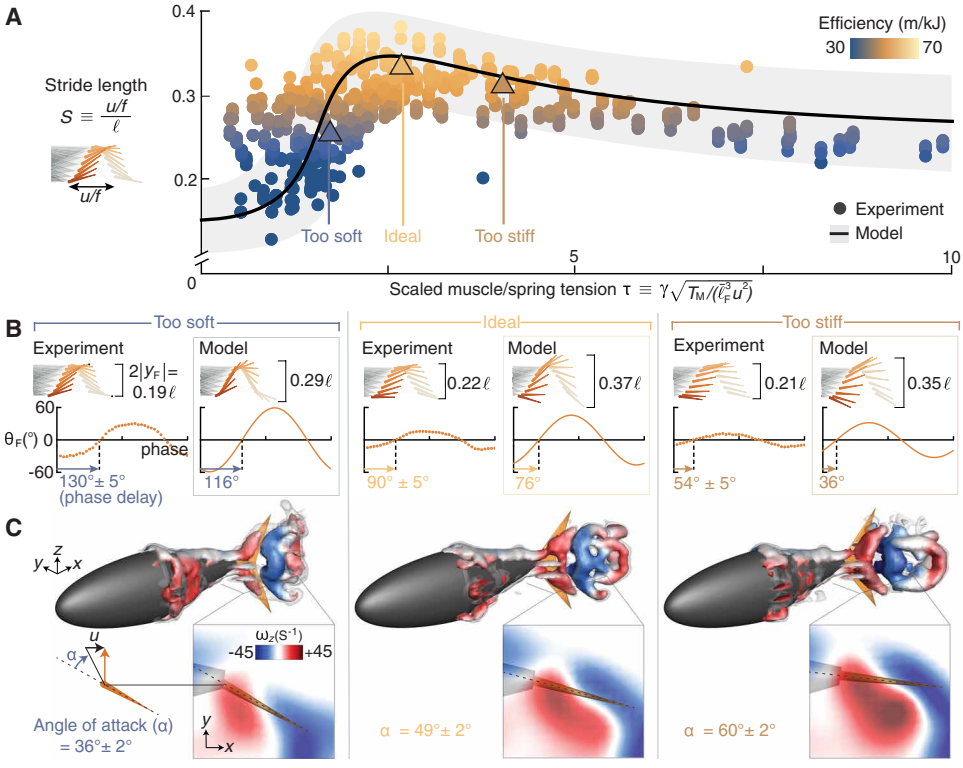

Fig. 3. Dimensional analysis and flow visualization reveal how muscle/spring tension affects dynamics. (**A**) Our model (black line) predicts that the scaled muscle tension (τ) determines the stride length (S) and thus the efficiency (see section S2.2). Experimental data (colored circles) support these predictions. Model is matched to experiment with a one-parameter fit for thrust coefficient ($C_T = 2.4$; see section S2.1). Shaded gray band shows the sensitivity of the fit ($C_T \pm 50\%$). (**B**) Three values of τ highlight differences in kinematics: too soft (τ =1.88), ideal (τ = 2.68), and too stiff (τ = 3.96) (f = 5 Hz; T_M = 1.6, 5.3, and 10.6 N). Tail fin traces illustrate how the phase relationships affect amplitude. (**C**) Increasing stiffness leads to higher angles of attack and a stronger, more detached LEV. Q-criterion isosurfaces are colored by dorsoventral vorticity (ω_z). Inserts: Top view of one slice at the tail fin's quarter span. See Materials and Methods and movie S2 for PIV details and animations.

In all cases, swimming was more efficient when stiffness was tunable rather than fixed. In the loose and rigid cases, the platform could not even reach the high speeds later in the mission (Fig. 4B). The medium case led to high efficiency by the end of the mission but low efficiency earlier in the mission (Fig. 4C). Only by tuning stiffness could the robot maintain a constant τ (Fig. 3A) and capture the benefits of flexibility over the full range of speeds. Tuning stiffness saved 16, 41, and 55% energy compared with the medium, rigid, and loose cases, respectively. Savings were comparable in the more complex missions (Fig. 4D). Although our model assumes a uniform incoming flow and small angles, it captures the basic trends of missions 3 and 4, where the platform maneuvered laterally and its tip-to-tip tail fin amplitude was 36°.

Tuning stiffness is most beneficial for high-frequency robots

Motivated by the energy savings we observed, we wondered how these savings scale with frequency and size according to our model. We considered fish-like robots with a maximum tailbeat frequency f_{max} and a tail fin length $\bar{\ell}_F$. Then, we calculated the average efficiency across frequencies ranging from 0 to f_{max}—first assuming the fixed stiffness that led to the highest average efficiency and then assuming tunable stiffness. We capped muscle tension at 240 N based on the elastic range of tuna tendons (*24*). We found that for small, slow-moving tails, tuning stiffness offers only marginal benefits because of the narrow range of optimal tensions (Fig. 5A). As tail fin size and frequency increase, fish-like robots have more to gain from tuning stiffness (energy savings rise to 20% as f_{max} rises to 10 Hz). Beyond some critical size and frequency, savings taper off as muscle strength becomes insufficient for creating the high tensions that optimize efficiency.

To corroborate our predictions of energy savings, we added fixed stiffness tail fins to the autonomous Tunabot (*9*) and tested it in our water channel. Despite measuring the efficiency differently (via the electrical power going to Tunabot), we found similar speed and efficiency trends to those observed on our platform (Figs. 2, A and B, and 5B), and the estimated energy savings of tuning stiffness were comparable with those predicted by our model (17 ± 5 versus 16%).

DISCUSSION

Our model and experimental data corroborate the same prediction: If stiffness does not increase with swimming speed squared, stride length and efficiency decrease. Although our robotic tests cannot prove whether fish use a particular tuning strategy, they offer a parsimonious explanation for trends observed in nature. In longnose gar (*Lepisosteus osseus*), artificially reducing stiffness caused fish to lower their tail-beat frequency (*44*). In pumpkinseed sunfish (*Lepomis gibbosus*), reducing stiffness led to lower swimming speeds at the same tail-beat frequency (*45*). Only by tuning stiffness could our platform and Tunabot maintain a linear frequency-speed relation and a plateaued frequency-efficiency relation using a single gait (Figs. 2 and 5B)—features that appear across several fish taxa (*25*, *32*, *46*–*49*).

Many aquatic vertebrates have caudal tendon arrangements analogous to that of tuna (*28*). Even sharks, distant relatives of tuna, are thought to stiffen their tail at high frequencies using their radialis muscle (*50*). Tuning stiffness may therefore be a widespread constraint for aquatic animals, which produce similar flexion ratios across a wide range of scales and speeds [e.g., clownfish up to humpback whales (*51*)]. Tuning is probably less important for small, low-frequency fins, where even a fixed stiffness can be near-optimal according to our model (Fig. 5A). Very large fins may also have limited use for tuning if the optimal stiffnesses are unattainable on the basis of available muscle strength (Fig. 5A). Although our savings estimates were based on tuna, this size constraint is likely more general, because the required tensions outpace strength as size scales up [modeled optimal tension scales with ℓ^3; muscle force scales with ℓ^2 (*52*)].

Although our stiffness-tuning model was inspired by tail fins, it could offer design insights to other fins or fluid-embedded devices.

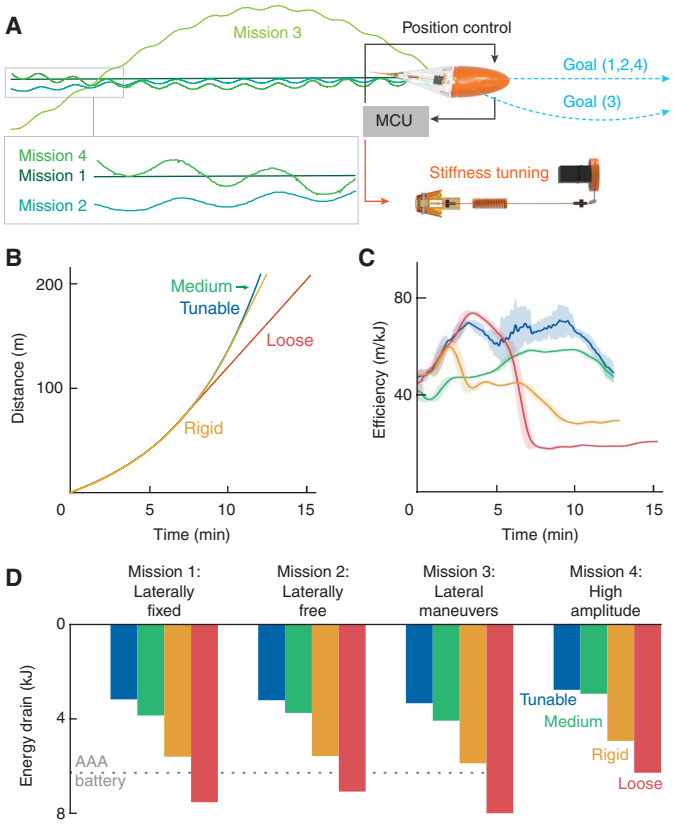

Fig. 4. Tuning stiffness saved energy across all missions. (**A**) The platform used closed-loop control to stay on its goal path [onboard PD controller in a microcontroller unit (MCU)]. (**B**) Tuning stiffness let the platform finish its mission faster. In the loose and rigid cases, speed plateaus during the mission. (**C**) Fixing stiffness led to inefficient mission segments. Only by tuning stiffness could the robotic tail maximize efficiency throughout the mission. (**D**) Tuning stiffness led to less energy drain in all four missions. Storage capacity of a AAA battery (≈ 6 kJ) is shown for reference. See Materials and Methods and movie S3 for details.

If the tendons were modeled on the side of the propulsor, rather than the leading edge, then the model could potentially approximate the pectoral fins of ray/skate-inspired robots, where the relative importance of active and passive control is an open question (*53*, *54*). Cantilever-based energy harvesters are also known to benefit from tunable stiffness, especially in dynamic flow environments (*55*, *56*). Because our model is derived from thin airfoil theory, it may be particularly relevant to harvesters that harness the aeroelastic vibrations of passive wings (*57*) or fluttering flags (*58*). In general, models that link stiffness tuning with performance can be used to produce known optimal kinematics (*3*–*7*) with existing stiffness-tuning mechanisms (*19*–*24*).

Regardless of how well our results apply to other systems, their implications for tuna-inspired robots are clear: Tuning flexibility is critical for efficient, multispeed operation. The latest tuna-inspired robots have huge frequency ranges: 0 to 15 Hz for Tunabot (*9*) and 0 to 20 Hz for iSplash (*11*). These vehicles may need to cruise for miles from a coastal outpost or ship and then slow down to navigate a coral reef or a narrow corridor. For these multifrequency, multispeed swimmers to maintain high efficiency, tuning flexibility may be as important as flexibility itself.

MATERIALS AND METHODS

Tuna tailfin joint stiffness tests

To measure the tail joint (peduncle) stiffness of tuna tails, we simulated loads on vertically mounted tuna tails ($n = 6$; fig. S1). For each tail, we dissected the peduncle to expose the lateral tendons and then hung weights from the tendons to prescribe the tendon tension (T_M). For each tension, we attached a second set of weights to the centerline distal tip of the caudal fin to simulate a lateral force (F_C). To account for fin asymmetries, we defined $F_C = 0$ where there was no lateral displacement.

The torque applied to the tail fin was $\ell_{laser}F_C$, where ℓ_{laser} was the perpendicular distance from the applied load to the axis on which the tail fin was mounted. For each combination of tendon tension and lateral force, we measured the displacement of the tail fin's centerline distal tip (Δd) using a laser distance sensor (±0.01 mm; fig. S1C). The corresponding approximated tail fin pitch angle was $\theta_F = \tan^{-1}(\Delta d/\ell_{laser})$. Each test was repeated three times.

Tuna-inspired platform design and fabrication

The basic shape of our platform follows our previous work on dorsal-caudal fin interactions (*59*), where we used videos of real yellowfin tuna to reconstruct a high-fidelity 3D model (*60*). We then simplified the surface shape and removed the keel, large dorsal fin, anal fin, pectoral fin, and finlets to isolate the effects of the tail fin. Our resulting reduced-order model is based on 11 critical measurements of the original high-fidelity tuna model and scaled to a whole-body length ℓ of 350 mm (fig. S2).

Our model was 3D-printed in parts: a fixed head, a tail frame, a tail shell, a tail joint, a tail fin connector, and a tail fin (fig. S2C). All parts except the tail joint were 3D-printed in nylon because it is naturally waterproof. To further waterproof the platform, we used silicone gel to seal the gap between the tail frame and shell (fig. S2C). The tail joint and tail fin connector were 3D-printed in stainless steel because of the high expected cyclical stresses.

To control the stiffness of the peduncle in real time, we installed a high-torque digital servo (Hitech HS-7245MG) inside the tail frame. The servo pulled on a polyethylene line (Spectra, 9.07-kg maximum load), which pulled on a linear spring, which pulled on the tail fin connector. The servo thus acted like an axial tendon that increased the effective torsional stiffness of the tail joint. Although real tuna have skeletal structures that limit tail joint angles, we omitted a mechanical stop to avoid any artificially imposed constraints on tail fin kinematics.

Tuna-inspired platform: Tethered testing protocols

To test the swimming performance of the tuna-inspired platform, we built a custom rig that suspended the platform into the 380 mm–by–450 mm–by–1520 mm ($W \times H \times L$) test section of a closed-loop water channel (0 to 1 m/s; Rolling Hills 1520). We used the rig for traditional force measurements, variable-speed semiautonomous missions, and 3D PIV.

To determine the platform's swimming speed, we used a Newton-Raphson zero-finding scheme. On the basis of preliminary tests of the actuator, we chose steady swimming speeds ranging from 100 to 700 mm/s (0.29 to 2 full body lengths/s) with 50-mm/s intervals. For each speed, we set the water channel to that speed and then sought the tailbeat frequency (f) that caused net thrust ($\overline{T}$) to be zero. The head of the platform was mounted independently from the tail, so the net thrust is the sum of the drag on the head (section S1.4) and the cycle-averaged streamwise force on the tail. After two initial

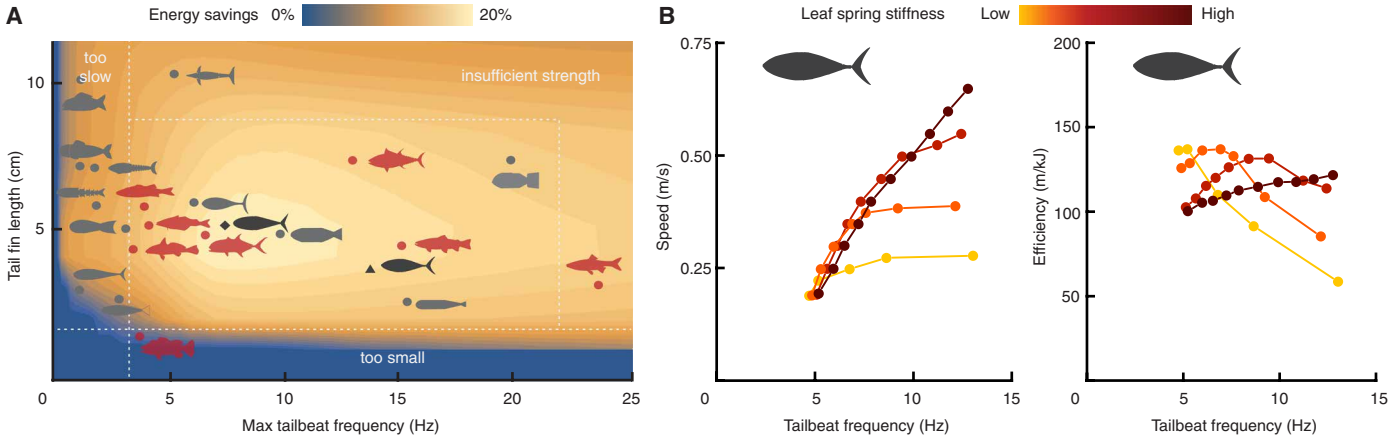

Fig. 5. Tunable stiffness is most beneficial for high-frequency robots. (**A**) Our model predicts that the benefits of tuning stiffness increase with frequency range, so long as robots are strong enough to produce the optimal stiffnesses. In platforms like ours (◆), or robots like Tunabot (▲), the model predicts efficiency savings up to 20%. Existing fish-like robots (●) and high-frequency fish (●) are shown for reference. Avatar descriptions are in table S1. (**B**) With fixed stiffness, Tunabot shows nonlinear speed-frequency and efficiency-frequency dependencies that are similar to those of our platform (Fig. 2, A and B). See section S1.5 for details.

guesses for f, the zero-finding scheme chose the next frequency as the intercept of a $f(\overline{T})$ line fitted through the two guess cases. This process repeated until the net thrust was lower than 5% of the static drag of the tail.

Each iteration of the scheme consisted of a standby period (10 s), a warm-up period (5 s), an effective data period (20 pitching cycles), a cool-down period (5 s), and a position neutralization period (fig. S4). The scheme repeated at each swimming speed, and each speed was repeated with 18 different spring tensions. Cases were omitted if the desired speed was unattainable at the maximum tailbeat frequency. Every combination of speed and tension was tested five times. The result is a function mapping frequency and stiffness to speed [$u(f, T_M)$; Fig. 2A].

To determine the platform's swimming efficiency, we divided speed by the average mechanical power consumption of the motor: $\xi \equiv u/\overline{p}_{\text{motor}}$. This ratio gives a measure of the model's range or distance traveled per unit energy. To estimate average mechanical power consumption, we derived an expression for motor power as a function of tail fin kinematics (section S1.3). The result is a function mapping frequency and stiffness to efficiency [$\xi(f, T_M)$; Fig. 2B].

Tuna-inspired platform: Untethered testing protocols

To simulate more realistic missions (Fig. 4 and fig. S7), we used air bushings to allow the platform to move freely in the horizontal plane. The bushings glided along horizontal stainless steel rails while two laser distance sensors measured the carriage's x and y position (fig. S6, A and B). Four independently controlled linear actuators raised/lowered each corner of the carriage support frame (1204 leadscrews with NEMA 57 stepper motors and braking clutches). We used the actuators to level the air bushing system to within ±0.001° before each experiment. The bushings were present in the speed and efficiency measurements (Fig. 2), but they were turned off and therefore nonfunctional.

To reduce extraneous forces on the carriage, we designed the system to be wireless. The carriage carried a battery and an onboard controller that transmitted all inputs/outputs wirelessly (Arduino Mega 2560 + XBee; ATI F/T wireless). The carriage carried a compressed air tank for the bushings (4500 psi, 1.47 liters), which it regulated with a programmable solenoid valve. We avoided latency differences between data channels by synchronizing all measurements on a custom A/D circuit before they were transmitted to our control PC (OMEN 870) (fig. S6C).

We used our air bushing setup to simulate four free-swimming missions. In each mission, the speed of the water channel increased from 0.1 to 0.65 m/s in intervals of 0.025 m/s. At each speed, the platform swam 9 m, resulting in a total distance of 207 m (the longest mission possible on one compressed air tank). The platform kept up with the incoming flow by controlling its frequency with an onboard PD controller (k_P = 0.05 Hz/cm, k_D = 2.53 Hz/cm per second).

The four missions were designed to test the robustness of the stiffness-tuning strategy; each considered a different modification (fig. S7C):

1) Mission 1. Streamwise (fore-aft) air bushings on. Platform is free to move forward/backward. A PD controller maintained the platform's speed by modulating frequency.

2) Mission 2. All air bushings on. Platform is free to move forward/backward/left/right. A second PD controller (k_P = 1° cm^{-1}, k_D = 1.18° s cm^{-1}) kept the platform centered in the channel by modulating pitch bias.

3) Mission 3. All air bushings on. A second PD controller kept the platform on a serpentine route [y_{goal} = 10 sin (0.1πt) cm] by modulating pitch bias.

4) Mission 4. All air bushings on. Tailbeat amplitude is 33% higher than missions 1 to 3. A second PD controller kept the platform centered in the channel by modulating pitch bias.

If the platform was unable to keep up with the flow, then the flow was coerced to the highest attainable speed. The loose stiffness case reached a maximum speed of 0.275 m/s, the rigid stiffness reached a maximum speed of 0.475 m/s, and the medium stiffness reached the highest requested speed (0.650 m/s) (fig. S7C). Speed limits were predetermined on the basis of Fig. 2A at 5.0 Hz so that unattainable speeds were not requested during the missions.

3D flow visualization

To visualize the flow around the platform, we captured 14 layers of stereo-PIV. The laser sheet stayed stationary while the leveling system

raised/lowered the carriage. The first layer was 5 mm (±2.5 μm) below the platform's midline, the next layer was 10 mm below the midline, etc. To avoid the wake of the driveshaft, we mirrored the bottom layers across a horizontal plane at the midline. The flow was seeded with neutrally buoyant seeding particles (polyamide, average diameter of 12 μm), which were illuminated by two overlapping laser sheets to avoid a tail shadow (5 W RayPower MGL-W-532; 10 W CNI MGL-W-532A). Two cameras beneath the channel recorded 2956 pixel–by–1877 pixel images of the particle motions (Phantom, SpeedSense M341).

To synchronize the cameras, we coupled a trigger signal with the encoder on the driveshaft. For each flow condition, the generator signaled the cameras to capture 40 equally spaced phases within each of 25 consecutive pitching cycles. The images were analyzed by an adaptive PIV algorithm (Dantec Dynamic Studio 6.5) using interrogation windows ranging from 16 pixels by 16 pixels to 64 pixels by 64 pixels with a 32 pixel–by–32 pixel grid step size. When creating wake isosurface plots (Fig. 4), we phase-averaged across pitching cycles. The phase averaging as well as the merging from 2D to 3D and the vorticity calculations were performed in MATLAB (2019a), and the 3D vorticity plots were created in Tecplot (2017R2).

SUPPLEMENTARY MATERIALS

robotics.sciencemag.org/cgi/content/full/6/57/eabe4088/DC1
Nomenclature
Sections S1 to S3
Figs. S1 to S10
Tables S1 to S3
Data file S1
Movies S1 to S3
References (*61*–*75*)

REFERENCES AND NOTES

1. G. V. Lauder, P. G. A. Madden, J. L. Tangorra, E. Anderson, T. V. Baker, Bioinspiration from fish for smart material design and function. *Smart Mater. Struct.* **20**, 94014 (2011).
2. J. H. Long, Muscles, elastic energy, and the dynamics of body stiffness in swimming eels. *Am. Zool.* **38**, 771–792 (1998).
3. T. Y. T. Wu, Hydromechanics of swimming of fishes and cetaceans. *Adv. Appl. Mech.* **11**, 1–63 (1971).
4. J. Katz, D. Weihs, Hydrodynamic propulsion by large amplitude oscillation of an airfoil with chordwise flexibility. *J. Fluid Mech.* **88**, 485–497 (1978).
5. S. Heathcote, I. Gursul, Flexible flapping airfoil propulsion at low reynolds numbers. *AIAA J.* **45**, 1066–1079 (2007).
6. J. L. Tangorra, G. V. Lauder, I. W. Hunter, R. Mittal, P. G. A. Madden, M. Bozkurttas, The effect of fin ray flexural rigidity on the propulsive forces generated by a biorobotic fish pectoral fin. *J. Exp. Biol.* **213**, 4043–4054 (2010).
7. C. J. Esposito, J. L. Tangorra, B. E. Flammang, G. V. Lauder, A robotic fish caudal fin: Effects of stiffness and motor program on locomotor performance. *J. Exp. Biol.* **215**, 56–67 (2012).
8. F. E. Fish, Advantages of aquatic animals as models for bio-inspired drones over present AUV technology. *Bioinspir. Biomim.* **15**, 025001 (2020).
9. J. Zhu, C. White, D. K. Wainwright, V. Di Santo, G. V. Lauder, H. Bart-Smith, Tuna robotics: A high-frequency experimental platform exploring the performance space of swimming fishes. *Sci. Robot.* **4**, eaax4615 (2019).
10. R. K. Katzschmann, J. DelPreto, R. MacCurdy, D. Rus, Exploration of underwater life with an acoustically controlled soft robotic fish. *Sci. Robot.* **3**, eaar3449 (2018).
11. R. J. Clapham, H. Hu, *iSplash*: Realizing fast Carangiform swimming to outperform a real fish. *Springer Tracts Mech. Eng.* **12**, 193–218 (2015).
12. A. R. Blight, The muscular control of vertebrate swimming movements. *Biol. Rev.* **52**, 181–218 (1977).
13. B. E. Flammang, G. V. Lauder, Speed-dependent intrinsic caudal fin muscle recruitment during steady swimming in bluegill sunfish, *Lepomis macrochirus*. *J. Exp. Biol.* **211**, 587–598 (2008).
14. J. H. Long Jr., K. S. Nipper, The importance of body stiffness in undulatory propulsion. *Am. Zool.* **36**, 678–694 (1996).
15. J. H. Long Jr., B. Adcock, R. G. Root, Force transmission via axial tendons in undulating fish: A dynamic analysis. *Comp. Biochem. Physiol. A Mol. Integr. Physiol.* **133**, 911–929 (2002).
16. K. Nguyen, N. Yu, M. M. Bandi, M. Venkadesan, S. Mandre, Curvature-induced stiffening of a fish fin. *J. R. Soc. Interface* **14**, 20170247 (2017).
17. M. Nakashima, K. Tokuo, K. Kaminaga, K. Ono, Experimental study of a self-propelled two-joint dolphin robot, in *Proceeding of the Ninth International Offshore and Polar Engineering Conference* (Brest, France, 1999).
18. J. H. Long Jr., T. J. Koob, K. Irving, K. Combie, V. Engel, N. Livingston, A. Lammert, J. Schumacher, Biomimetic evolutionary analysis: Testing the adaptive value of vertebrate tail stiffness in autonomous swimming robots. *J. Exp. Biol.* **209**, 4732–4746 (2006).
19. M. Ziegler, M. Hoffmann, J. P. Carbajal, R. Pfeifer, Varying body stiffness for aquatic locomotion, in *Proceedings of the 2011 IEEE International Conference on Robotics and Automation* (IEEE, Shanghai, China, 9 to 13 May 2011), pp. 2705–2712.
20. M. Nakabayashi, R. Kobayashi, S. Kobayashi, H. Morikawa, Bioinspired propulsion mechanism using a fin with a dynamic variable-effective-length spring: Evaluation of thrust characteristics and flow around a fin in a uniform flow. *J. Biomech. Sci. Eng.* **4**, 82–93 (2009).
21. A. Jusufi, D. M. Vogt, R. J. Wood, G. V. Lauder, Undulatory swimming performance and body stiffness modulation in a soft robotic fish-inspired physical model. *Soft Robot.* **4**, 202–210 (2017).
22. Y. J. Park, T. M. Huh, D. Park, K. J. Cho, Design of a variable-stiffness flapping mechanism for maximizing the thrust of a bio-inspired underwater robot. *Bioinspir. Biomim.* **9**, 036002 (2014).
23. S. B. Behbahani, X. Tan, Design and dynamic modeling of electrorheological fluid-based variable-stiffness fin for robotic fish. *Smart Mater. Struct.* **26**, 085014 (2017).
24. J. Yu, Z. Su, Z. Wu, M. Tan, Development of a fast-swimming dolphin robot capable of leaping. *IEEE/ASME Trans. Mechatron.* **21**, 2307–2316 (2016).
25. F. Fish, G. V. Lauder, Passive and active flow control by swimming fishes and mammals. *Annu. Rev. Fluid Mech.* **38**, 193–224 (2006).
26. R. E. Shadwick, D. A. Syme, Thunniform swimming: Muscle dynamics and mechanical power production of aerobic fibres in yellowfin tuna (Thunnus albacares). *J. Exp. Biol.* **211**, 1603–1611 (2008).
27. D. K. Wainwright, G. V. Lauder, Tunas as a high-performance fish platform for inspiring the next generation of autonomous underwater vehicles. *Bioinspir. Biomim.* **15**, 35007 (2020).
28. R. E. Shadwick, H. S. Rapoport, J. M. Fenger, Structure and function of tuna tail tendons. *Comp. Biochem. Physiol. A Mol. Integr. Physiol.* **133**, 1109–1125 (2002).
29. M. H. Dickinson, C. T. Farley, R. J. Full, M. A. R. Koehl, R. Kram, S. Lehman, How animals move: An integrative view. *Science* **288**, 100–106 (2000).
30. D. A. Pabst, Springs in swimming animals. *Am. Zool.* **36**, 723–735 (1996).
31. J. Katz, A. Plotkin, *Low-Speed Aerodynamics* (Cambridge Univ. Press, 2001), vol. 13.
32. R. Bainbridge, The speed of swimming of fish as related to size and to the frequency and amplitude of the tail beat. *J. Exp. Biol.* **35**, 109–133 (1958).
33. M. J. Lighthill, Aquatic animal propulsion of high hydromechanical efficiency. *J. Fluid Mech.* **44**, 265 (1970).
34. I. E. Garrick, Propulsion of a flapping and oscillating airfoil, in *National Advisory Committee for Aeronautics* (NACA Technical Reports, 1936), pp. 419–427.
35. L. I. Sedov, *Similarity and Dimensional Methods in Mechanics* (CRC Press, 1993).
36. E. D. Tytell, M. C. Leftwich, C.-Y. Hsu, B. E. Griffith, A. H. Cohen, A. J. Smits, C. Hamlet, L. J. Fauci, Role of body stiffness in undulatory swimming: Insights from robotic and computational models. *Phys. Rev. Fluids* **1**, 73202 (2016).
37. T. Van Buren, D. Floryan, A. J. Smits, Scaling and performance of simultaneously heaving and pitching foils. *AIAA J.* **57**, 3666–3677 (2019).
38. D. B. Quinn, G. V. Lauder, A. J. Smits, Maximizing the efficiency of a flexible propulsor using experimental optimization. *J. Fluid Mech.* **767**, 430–448 (2015).
39. W. Weaver Jr, S. P. Timoshenko, D. H. Young, *Vibration Problems in Engineering* (John Wiley & Sons, 1990).
40. J. D. Eldredge, A. R. Jones, Leading-edge vortices: Mechanics and modeling. *Annu. Rev. Fluid Mech.* **51**, 75–104 (2019).
41. I. Borazjani, M. Daghooghi, The fish tail motion forms an attached leading edge vortex. *Proc. R. Soc. B* **280**, 20122071 (2013).
42. Z. J. Wang, Vortex shedding and frequency selection in flapping flight. *J. Fluid Mech.* **410**, 323–341 (2000).
43. G. C. Lewin, H. Haj-Hariri, Modelling thrust generation of a two-dimensional heaving airfoil in a viscous flow. *J. Fluid Mech.* **492**, 339–362 (2003).
44. J. H. Long Jr., M. E. Hale, M. J. McHenry, M. W. Westneat, Functions of fish skin: Flexural stiffness and steady swimming of longnose gar, *Lepisosteus osseus*. *J. Exp. Biol.* **1999**, 2139–2151 (1996).
45. J. H. Long Jr., M. Mchenry, N. Boetticher, Undulatory swimming: How traveling waves are produced and modulated in sunfish (*Lepomis Gibbosus*). *J. Exp. Biol.* **192**, 129–145 (1994).
46. J. R. Hunter, Sustained speed of jack mackerel, *Trachurus symmetricus*. *Fish. Bull.* **69**, 267–271 (1971).

47. J. M. Blank, C. J. Farwell, J. M. Morrissette, R. J. Schallert, B. A. Block, *Influence of Swimming Speed on Metabolic Rates of Juvenile Pacific Bluefin Tuna and Yellowfin Tuna* (2007); www.journals.uchicago.edu/t-and-c.
48. R. E. Shadwick, S. Gemballa, Structure, kinematics, and muscle dynamics in undulatory swimming. *Fish Physiol.* **23**, 241–280 (2005).
49. V. Di Santo, C. P. Kenaley, G. V. Lauder, High postural costs and anaerobic metabolism during swimming support the hypothesis of a U-shaped metabolism–speed curve in fishes. *Proc. Natl. Acad. Sci. U.S.A.* **114**, 13048–13053 (2017).
50. B. E. Flammang, Functional morphology of the radialis muscle in shark tails. *J. Morphol.* **271**, 340–352 (2010).
51. K. N. Lucas, N. Johnson, W. T. Beaulieu, E. Cathcart, G. Tirrell, S. P. Colin, B. J. Gemmell, J. O. Dabiri, J. H. Costello, Bending rules for animal propulsion. *Nat. Commun.* **5**, 3293 (2014).
52. T. A. McMahon, *Muscles, Reflexes, and Locomotion* (Princeton Univ. Press, 1984).
53. F. Fish, C. Schreiber, K. Moored, G. Liu, H. Dong, H. Bart-Smith, Hydrodynamic performance of aquatic flapping: Efficiency of underwater flight in the manta. *Aerospace* **3**, 20 (2016).
54. Y. Cai, S. Bi, L. Zheng, Design optimization of a bionic fish with multi-joint fin rays. *Adv. Robot.* **26**, 177–196 (2012).
55. V. R. Challa, M. G. Prasad, Y. Shi, F. T. Fisher, A vibration energy harvesting device with bidirectional resonance frequency tunability. *Smart Mater. Struct.* **17**, 015035 (2008).
56. T. W. Secord, M. C. Audi, A tunable resonance cantilever for cardiac energy harvesting. *Cardiovasc. Eng. Technol.* **10**, 380–393 (2019).
57. Y. Zhu, Y. Su, K. Breuer, Nonlinear flow-induced instability of an elastically mounted pitching wing. *J. Fluid Mech.* **899**, A35 (2020).
58. K. Shoele, R. Mittal, Energy harvesting by flow-induced flutter in a simple model of an inverted piezoelectric flag. *J. Fluid Mech.* **790**, 582–606 (2016).
59. Q. Zhong, H. Dong, D. B. Quinn, How dorsal fin sharpness affects swimming speed and economy. *J. Fluid Mech.* **878**, 370–385 (2019).
60. G. Liu, Y. Ren, H. Dong, O. Akanyeti, J. C. Liao, G. V. Lauder, Computational analysis of vortex dynamics and performance enhancement due to body–fin and fin–fin interactions in fish-like locomotion. *J. Fluid Mech.* **829**, 65–88 (2017).
61. V. Kopman, J. Laut, F. Acquaviva, A. Rizzo, M. Porfiri, Dynamic modeling of a robotic fish propelled by a compliant tail. *IEEE J. Ocean. Eng.* **40**, 209–221 (2015).
62. S. Fujiwara, S. Yamaguchi, Development of fishlike robot that imitates carangiform and subcarangiform swimming motions. *J. Aero Aqua Biomech.* **6**, 1–8 (2017).
63. Y. Zhong, Z. Li, R. Du, The design and prototyping of a wire-driven robot fish with pectoral fins, in *Proceedings of the 2013 IEEE International Conference on Robotics and Biomimetics, (ROBIO)* (IEEE, 2013), pp. 1918–1923.
64. J. Shintake, V. Cacucciolo, H. Shea, D. Floreano, Soft biomimetic fish robot made of dielectric elastomer actuators. *Soft Robot.* **5**, 466–474 (2018).
65. S. F. Masoomi, S. Gutschmidt, X. Q. Chen, M. Sellier, The kinematics and dynamics of undulatory motion of a tuna-mimetic robot. *Int. J. Adv. Robot. Syst.* **12**, 1–11 (2015).
66. J. Yu, C. Zhang, L. Liu, Design and control of a single-motor-actuated robotic fish capable of fast swimming and maneuverability. *IEEE/ASME Trans. Mechatron.* **21**, 1711–1719 (2016).
67. S. C. van den Berg, thesis, Delft University of Technology (2019).
68. J. Herskin, J. F. Steffensen, Energy savings in sea bass swimming in a school: Measurements of tail beat frequency and oxygen consumption at different swimming speeds. *J. Fish Biol.* **53**, 366–376 (1998).
69. M. F. Steinhausen, J. F. Steffensen, N. G. Andersen, Tail beat frequency as a predictor of swimming speed and oxygen consumption of saithe (*Pollachius virens*) and whiting (*Merlangius merlangus*) during forced swimming. *Marine Biol.* **148**, 197–204 (2005).
70. H. S. H. Yuen, Swimming speeds of yellowfin and skipjack tuna. *Trans. Am. Fish. Soc.* **95**, 203–209 (1966).
71. K. A. Dickson, J. M. Donley, M. W. Hansen, J. A. Peters, Maximum sustainable speed, energetics and swimming kinematics of a tropical carangid fish, the green jack Caranx caballus. *J. Fish Biol.* **80**, 2494–2516 (2012).
72. K. L. Feilich, Swimming with multiple propulsors: Measurement and comparison of swimming gaits in three species of neotropical cichlids. *J. Exp. Biol.* **220**, 4242–4251 (2017).
73. J. Yu, M. Tan, S. Wang, E. Chen, Development of a biomimetic robotic fish and its control algorithm. *IEEE Trans. Syst. Man Cybern. B.* **34**, 1798–1810 (2004).
74. J. Liu, H. Hu, Biological inspiration: From carangiform fish to multi-joint robotic fish. *J. Bionic Eng.* **7**, 35–48 (2010).
75. D. Floryan, T. Van Buren, C. W. Rowley, A. J. Smits, Scaling the propulsive performance of heaving and pitching foils. *J. Fluid Mech.* **822**, 386–397 (2017).

Acknowledgments: We would like to thank G. Lauder for helpful advice and feedback and W. Wang for assistance with prototyping. **Funding:** This work was made possible by funding from the Office of Naval Research (N00014-14-1-0533, N00014-18-1-2537, and N00014-08-1-0642; Program Manager: R. Brizzolara), the NSF (1921809 and 2040351; Program Manager: R. Joslin), and the University of Virginia. **Author contributions:** All authors contributed to the concept of the study and reviewed the manuscript. Q.Z. built and collected data with the tuna-inspired water channel platform. Q.Z., F.E.F., S.J.K., and A.M.D. built and collected data with the tuna tail tensioning rig. Q.Z. and J.Z. modified and collected data with Tunabot. Q.Z. and D.B.Q. designed the experiments, analyzed the data, developed the hydrodynamic model, made the figures, and drafted the manuscript. H.B.-S., F.E.F., and D.B.Q. acquired funding for the research. F.E.F. supervised the tuna tail testing; H.B.-S. supervised Tunabot construction; D.B.Q. supervised the tuna-inspired platform tests and the mathematical modeling. **Competing interests:** The authors declare that they have no competing interests. **Data and materials availability:** All data are available in the main text or the Supplementary Materials.

Submitted 19 August 2020
Accepted 20 July 2021
Published 11 August 2021
10.1126/scirobotics.abe4088

Citation: Q. Zhong, J. Zhu, F. E. Fish, S. J. Kerr, A. M. Downs, H. Bart-Smith, D. B. Quinn, Tunable stiffness enables fast and efficient swimming in fish-like robots. *Sci. Robot.* **6**, eabe4088 (2021).

Science Robotics

Tunable stiffness enables fast and efficient swimming in fish-like robots

Q. ZhongJ. ZhuF. E. FishS. J. KerrA. M. DownsH. Bart-SmithD. B. Quinn

Sci. Robot., 6 (57), eabe4088. • DOI: 10.1126/scirobotics.abe4088

Science Robotics (ISSN) is published by the American Association for the Advancement of Science. 1200 New York Avenue NW, Washington, DC 20005. The title *Science Robotics* is a registered trademark of AAAS.